

This document is the Accepted Manuscript version of a Published Work that appeared in final form in *Journal of the American Chemical Society*, copyright © American Chemical Society after peer review and technical editing by the publisher. To access the final edited and published work see:
<https://dx.doi.org/10.1021/jacs.9b12389>.

Biomimetic synthesis of sub-20 nanometer Covalent Organic Frameworks in water

Authors

Carlos Franco^{1†}, David Rodríguez-San-Miguel^{2†}, Alessandro Sorrenti¹, Semih Sevim¹, Ramon Pons³, Ana E. Platero-Prats², Marko Pavlovic^{4,5}, Istvan Szilágyi^{4,6}, M. Luisa Ruiz Gonzalez⁷, José M. González-Calbet⁷, Davide Bochicchio⁸, Luca Pesce⁸, Giovanni M. Pavan⁸, Inhar Imaz⁹, Mary Cano-Sarabia⁹, Daniel Maspoch^{9,10}, Salvador Pané¹¹, Andrew J. deMello¹, Felix. Zamora^{2*}, Josep Puigmartí-Luis^{1*}

Affiliations

¹Department of Chemistry and Applied Biosciences, Institute for Chemical and Bioengineering, ETH Zurich, Vladimir Prelog Weg 1, 8093 Zurich, Switzerland.

²Departamento de Química Inorgánica, Institute for Advanced Research in Chemical Sciences (IAdChem) and Condensed Matter Physics Institute (IFIMAC). Universidad Autónoma de Madrid, 28049 Madrid, Spain.

³Institute for Advanced Chemistry of Catalonia (IQAC-CSIC), Jordi Girona 18-26, E-08034 Barcelona, Spain.

⁴MTA-SZTE Lendület Biocolloids Research Group, University of Szeged, H-6720 Szeged, Hungary.

⁵Max-Planck Institute of Colloids and Interfaces; Department of Colloid Chemistry, Am Mühlenberg 1, 14476 Potsdam, Germany

⁶Interdisciplinary Excellence Center, Department of Physical Chemistry and Materials Science, University of Szeged, H-6720 Szeged, Hungary.

⁷Departamento de Química Inorgánica, Universidad Complutense de Madrid, 28040 Madrid, Spain.

⁸Department of Innovative Technologies, University of Applied Sciences and Arts of Southern Switzerland, Galleria 2, Via Cantonale 2c, CH-6928 Manno, Switzerland.

⁹Catalan Institute of Nanoscience and Nanotechnology (ICN2), CSIC and BIST Campus UAB, Bellaterra, 08193 Barcelona, Spain.

¹⁰ICREA, Pg. Lluís Companys 23, 08010 Barcelona, Spain.

¹¹Multi-Scale Robotics Lab ETH Zurich Tannenstrasse 3, CH-8092 Zurich, Switzerland.

*Correspondence to: felix.zamora@uam.es, jpuigmarti@ethz.ch

† These authors contributed equally to this work.

37 **Abstract**

38 Covalent organic frameworks (COFs) are commonly synthesized under harsh conditions yielding
39 unprocessable powders. Control in their crystallization process and growth has been limited to
40 studies conducted in hazardous organic solvents. Herein, we report a one-pot synthetic method that
41 yields stable aqueous colloidal solutions of sub-20 nm crystalline imine-based COF particles at
42 room temperature and ambient pressure. Additionally, through the combination of experimental
43 and computational studies, we investigated the mechanisms and forces underlying the formation of
44 such imine-based COF colloids in water. Further, we show that our method can be used to process
45 the colloidal solution into 2D and 3D COF shapes, as well as to generate a COF ink that can be
46 directly printed onto surfaces. These findings should open new vistas in COF chemistry enabling
47 new application areas.

48

49 **Introduction**

50 Covalent organic frameworks (COFs) are porous crystalline materials generated from organic
51 molecules linked via reversible covalent bonds.¹ Since its discovery, COF chemistry has facilitated
52 a modular construction of periodic crystalline matter by connecting molecular subunits in a
53 predictable and modular fashion.² This strategy has proved efficient in generating extended
54 crystalline and porous networks possessing permanent porosity, high specific surface areas and
55 excellent thermal/chemical stability; features that have found potential applications in a vast
56 number of fields.³ However, conventional routes for COF synthesis involve high temperatures,
57 which when combined with the low solubility of the initial building blocks in common reaction
58 media, yield poor control over the size of the crystalline domains and the morphology of COF
59 crystals.⁴ Unsurprisingly, such drawbacks have hampered the extraction of reliable information
60 regarding the effects of crystallite size and morphology on COF properties. Accordingly, much

61 effort is now focused on both understanding and controlling the growth of COF crystals at length
62 scales spanning the nanometer to micron scales.

63 Recently, Dichtel and co-workers reported on the preparation of stable particles of boronate ester-
64 linked COFs, whose size can be modulated between 40 and hundreds of nanometers by using
65 mixtures of organic solvents at high temperature.⁵ Later, such COFs colloidal solutions in organic
66 media have been used by the same authors for preparing micron-sized single crystals of boronate
67 ester-linked COFs via a seeded growth procedure.⁶ Therefore, having access to nanometer-sized
68 particles of COFs allowed the authors to overcome a long-standing challenge in the field, i.e. the
69 formation of large single crystals of COFs. Besides this specific example, COF crystal-downsizing
70 will be key to transforming COFs from unprocessable crystalline powders into processable
71 materials, integrating COFs into nanoscale devices,⁷ as well as establishing relationships between
72 COF crystal size and properties. In addition, COF crystal downsizing will expand the range of
73 applications of these materials, such as in the biomedical, device and printing arenas,⁸ and enhance
74 their bioavailability.⁹ However, only nanoparticles of boronate ester-linked COFs in organic
75 solvents have been reported so far.⁵ Unfortunately, boron-based COFs have poor chemical
76 stabilities, which limits their practical implementation. In addition, the fact that hazardous organic
77 solvents are still required as a medium to stabilize their colloidal dispersion precludes their use in
78 biological environments. In contrast, imine-based COFs are significantly more stable and robust
79 for practical use.¹⁰ Nevertheless, despite the high number of reports on imine-based COFs, it has
80 not been possible yet to downsize them to the nanoscale.¹¹ Put simply, routes for producing aqueous
81 colloidal solutions of imine-linked COF nanoparticles are still missing.

82 To overcome this limitation, we report here an efficient one-pot method to generate stable and
83 homogeneous colloidal solutions of sub-20 nanometer imine-linked COF particles in water. The

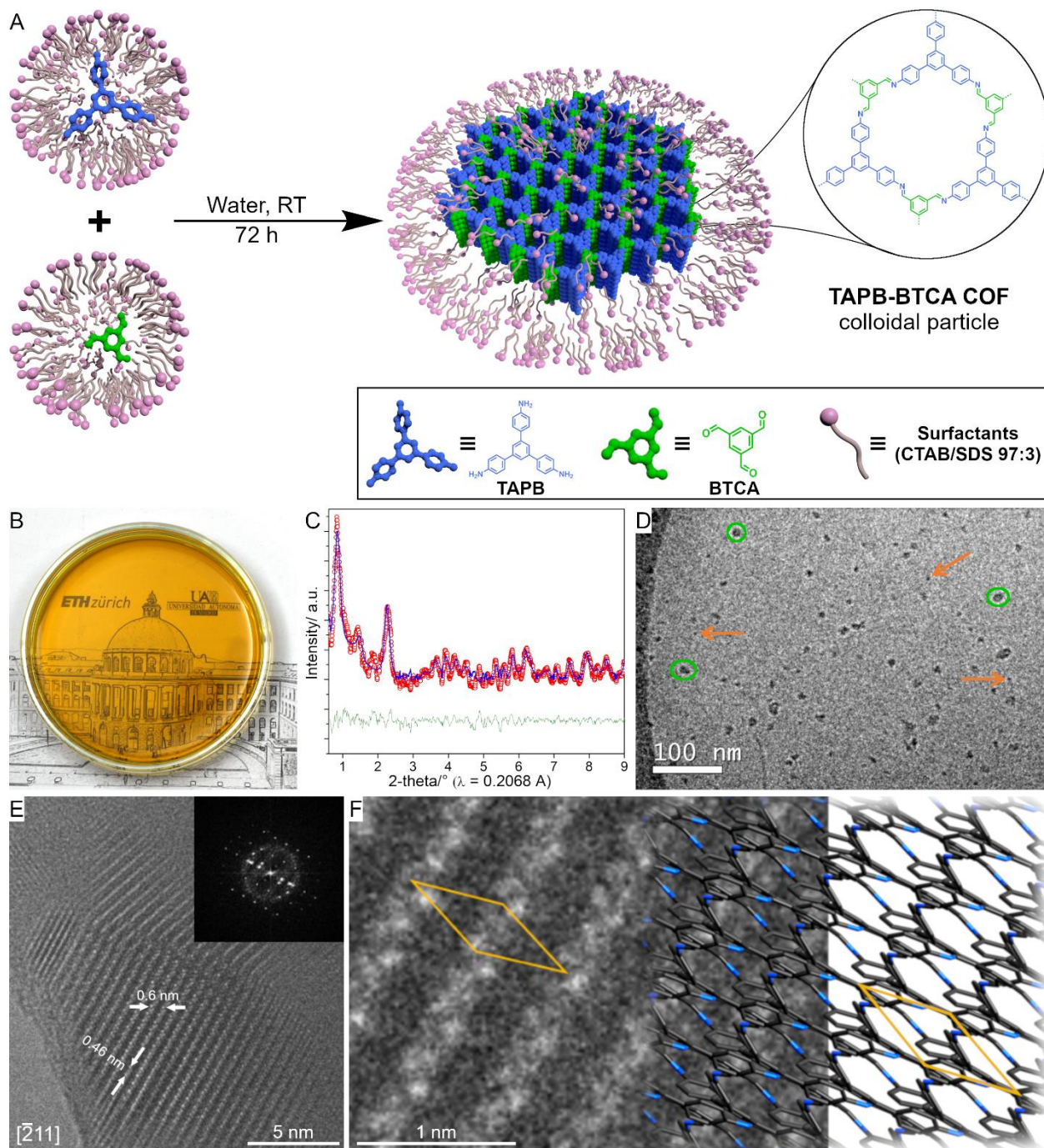
84 synthesis of crystalline COF colloids was performed for the first time at room temperature using
85 micelles as reaction nanocompartments. This approach was inspired by living systems that make
86 use of confined volumes (such as intracellular compartments) to control crystallization processes
87 in aqueous media.^{12–14} This method allowed us to use a combination of experimental scattering
88 techniques in solution, that together with computational calculations, gave unprecedented insights
89 into the mechanism and forces underlying the formation of imine-linked COFs. Additionally, we
90 show that the produced colloids enable the processing of COFs into 2D and 3D shapes such as
91 crystalline freestanding films and monoliths. Further, we prove that such colloids can also be used
92 as inks to directly print COFs onto surfaces. Finally, we demonstrated the generality of our method
93 by applying it to the synthesis of metal-organic frameworks (MOFs) colloids. In particular, we
94 show the synthesis of 20 nanometer MIL-100(Fe) particles at room temperature and ambient
95 pressure. MIL-100(Fe) is a prototypical MOF that requires harsh conditions for its synthesis¹⁵ and
96 only forms larger crystals.¹⁶ We expect that the presented methodology will vastly increase
97 knowledge on structure-property correlations in COFs and MOFs, allowing access to a large
98 number of new applications and functions, whilst significantly enhancing the bioavailability and
99 processability of these materials.

100 **Results**

101 **TAPB-BTCA COF** is typically obtained via imine condensation between 1,3,5-tris(4-
102 aminophenyl)benzene (**TAPB**) and 1,3,5-triformylbenzene (**BTCA**) in *meta*-cresol or DMSO.
103 Additionally, acetic acid is used as a catalyst to yield **TAPB-BTCA COF** as an insoluble and
104 unprocessable crystalline powder.¹⁷ Herein, we employed the *catanionic* micellar system^{18,19}
105 formed from a mixture of cationic hexadecyltrimethylammonium bromide (CTAB) and anionic
106 sodium dodecyl sulfate (SDS) surfactants (CTAB/SDS 97:3) to generate stable colloidal solutions

107 of crystalline **TAPB-BTCA COF** nanoparticles in water (**Fig. 1A**). Note that this surfactant ratio
108 guarantees the formation of small mixed micelles in the *catanionic* mixture, instead of bigger
109 vesicles as previously reported,¹⁸ and here it was optimized to achieve the smallest size of **TAPB-**
110 **BTCA COF** nanoparticles (**Fig. S1**). The micellar medium allows the solubilization in water of
111 the otherwise insoluble molecular building blocks **BTCA** and **TAPB** at room temperature, yielding
112 two homogeneous solutions of the reactants loaded into CTAB/SDS mixed micelles.²⁰ After
113 mixing the solutions and adding acetic acid, the reaction mixture turned orange, indicating the
114 formation of imine bonds characteristic of **TAPB-BTCA COF** growth. However, and in contrast
115 to observations in standard synthetic protocols, the reaction mixture remained clear and
116 homogeneous with no apparent precipitation (**Fig. 1B**), even after storage at room temperature for
117 twelve months (**Fig. S3**). Indeed, when irradiated with a laser ($\lambda = 630$ nm), the reaction mixture
118 clearly exhibited Willis–Tyndall scattering behavior,²¹ confirming the presence of colloidal
119 particles (**Fig. S2**). To validate the existence of crystalline **TAPB-BTCA COF** nanoparticles in the
120 reaction mixture, synchrotron X-ray diffraction measurements were performed directly on the
121 colloidal solution generated after mixing. The experimental differential diffraction data were fitted
122 using the Le Bail method^{22,23} against the reported structural model for **TAPB-BTCA COF** (*P3*, a
123 ~ 15.91 Å and $c \sim 3.54$ Å as refined cell parameters) (**Fig. 1C**), demonstrating the presence of the
124 crystalline COF phase with a main low-angle peak centered at 0.86° 2-theta values ($\lambda = 0.2068$ Å)
125 associated with the (100) Bragg reflection.¹⁷ Accordingly, this result unambiguously confirmed the
126 formation of crystalline **TAPB-BTCA COF** nanoparticles via the mixed micelle method. The sizes
127 and morphology of the obtained **TAPB-BTCA COF** nanoparticles were subsequently studied by
128 dynamic light scattering (DLS) and cryogenic transmission electron microscopy (cryo-TEM). DLS
129 measurements conducted on the reaction mixture after 24 hours (**Fig. S3A**) reported a
130 monodisperse distribution of scatterers centred at 16 nm. Remarkably, the colloidal behaviour of

131 the reaction mixture remains stable and homogeneous (with no appreciable turbidity or size
132 increase) for periods in excess of six months (**Fig. S3B**). Additionally, cryo-TEM images of the
133 reaction mixture after 24 hours (**Fig. 1D**) showed two different populations of objects; one centred
134 at 5 ± 1 nm and the other at 16 ± 1 nm in diameter. The former value correlated well with the size of
135 surfactant micelles determined by small-angle X-ray scattering (SAXS) in the pure CTAB/SDS
136 (97:3) mixture (see below and **Fig. S11**), with the latter comparing well with the size distribution
137 measured by DLS, and thus being ascribed to **TAPB-BTCA COF** nanoparticles. The high-
138 resolution transmission electron microscopy (HR-TEM) study of drop cast reaction mixtures
139 further confirmed the crystallinity of **TAPB-BTCA COF** nanoparticles. **Fig. 1E** shows a
140 characteristic HRTEM image and its corresponding Fast Fourier Transform (FFT). The measured
141 periodicities (white arrows in **Fig. 1E**) match well with the unit cell geometry of **TAPB-BTCA**
142 **COF** as viewed along the $[-211]$ zone axis. **Fig. 1F** presents a magnified detail of the above HR-
143 TEM image overlapped with the simulated crystal structure of **TAPB-BTCA COF** viewed along
144 the $[-211]$ zone axis, suggesting a good match between the light and dark fringes of the micrograph
145 and the higher and lower atomic density regions of the COF structure. Additionally, scanning
146 electron microscopy (SEM) images of drop cast reaction mixtures revealed the presence of well-
147 defined and uniform nanoparticles (and nanoparticle clusters), with a size that correlates well with
148 both DLS and cryo-TEM measurements (**Fig. S1A**).



149

150 **Fig. 1. TAPB-BTCA COF nanoparticles.** (A) Schematic representation of the synthesis of colloidal TAPB-BTCA

151 COF nanoparticles in water. (B) Photograph of the transparent reaction mixture. (C) Synchrotron X-ray diffraction

152 pattern of the reaction mixture containing TAPB-BTCA COF nanoparticles. Experimental differential data are shown

153 in red, with the calculated fit using $P3$, $a \sim 15.91 \text{ \AA}$ and $c \sim 3.54 \text{ \AA}$ as refined cell parameters in blue and associated

154 residuals in green. (D) Cryo-TEM image of TAPB-BTCA COF colloid. For clarity, some TAPB-BTCA COF

155 nanoparticles are outlined in green and some micelles are indicated by orange arrows. (E) HR-TEM image of a TAPB-

156 **BTCA COF** nanoparticle along the [-211] zone axis, with the inset showing the FFT. (F) Magnified HR-TEM image
157 of a defined area in (E) overlaid with the schematic structural model of **TAPB-BTCA COF** along the [-211] projection.
158

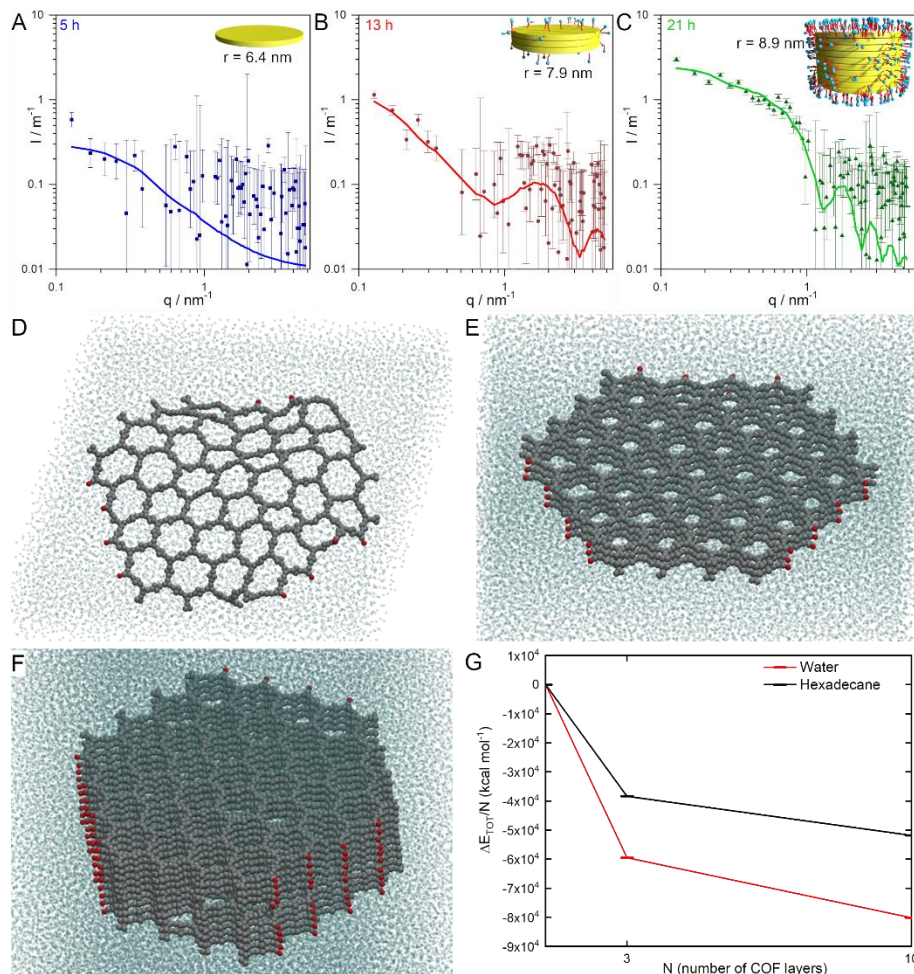
159 After confirming that sub-20 nanometer **TAPB-BTCA COF** particles can be generated, we
160 investigated the possibility of isolating the COF material as a bulk solid. To this purpose, , we
161 added ethanol to the reaction mixture to destabilize the surfactant aggregates,²⁴ which triggered the
162 flocculation of **TAPB-BTCA COF** nanoparticles as an insoluble yellow powder, hereafter termed
163 **TAPB-BTCA COF(s)**. After flocculation, **TAPB-BTCA COF(s)** could be simply isolated from
164 the reaction mixture by centrifugation. **TAPB-BTCA COF(s)** was characterized by Fourier-
165 transform infrared (FT-IR) spectroscopy and solid-state Cross Polarization/Magic Angle Spinning
166 Nuclear Magnetic Resonance (¹³C CP-MAS NMR). FT-IR spectra confirmed the presence of imine
167 bonds through the appearance of the characteristic imine C=N stretching band at 1623 cm⁻¹ (**Fig.**
168 **S4**), while solid state ¹³C CP-MAS NMR spectra exhibited the representative signal of the imine
169 carbon atom at 157.1 ppm (**Fig. S5**). Additionally, powder X-ray diffraction (PXRD) patterns of
170 **TAPB-BTCA COF(s)** (**Fig. S6**) were in excellent accordance with those previously reported for
171 this material.¹⁷ It should be noted that the measured PXRD peaks were broader than those usually
172 observed for **TAPB-BTCA COF(s)** prepared by conventional bulk synthetic methods,¹¹
173 suggesting the presence of smaller crystalline domains in **TAPB-BTCA COF(s)**.²⁵ The permanent
174 porosity of **TAPB-BTCA COF(s)** was also confirmed by nitrogen adsorption isotherm
175 measurements on previously activated samples, showing a characteristic isotherm with a Brunauer–
176 Emmet–Teller (BET) area (A_{BET}) of 687 m² g⁻¹ at 77 K (**Fig. S7**). Finally, the CO₂ and water
177 sorption properties of **TAPB-BTCA COF(s)** were also measured (**Fig. S8** and **S9**). It was found
178 to be porous to CO₂ with a total uptake of 9 mmol g⁻¹ at 203 K and 760 torr (1 mmol g⁻¹ at 298 K
179 and 760 torr). Moreover, water-vapour sorption isotherms showed a step between 40-50% relative

180 humidity, after which the water uptake increases monotonically until a maximum of 15% in mass
181 ($0.15 \text{ g}_{\text{water}} \text{ g}_{\text{COF}}^{-1}$), which is the typical behaviour for this class of materials bearing hydrophobic
182 walls.¹¹

183 To clarify the processes underlying the formation of **TAPB-BTCA COF** nanoparticles in the
184 *catanionic* micellar medium, time-resolved *in-situ* DLS and SAXS experiments were performed.
185 DLS indicated that the average hydrodynamic diameter of colloidal particles increased during the
186 first few hours (after the addition of acetic acid), leveling off to yield a final average hydrodynamic
187 diameter of 16 nm (**Fig. S10**). In contrast, when the synthesis was performed in pure CTAB
188 micelles (*i.e.* without SDS), the size of **TAPB-BTCA COF** continued to increase until precipitation
189 occurred. Accordingly, the role of the anionic surfactant was clearly evidenced, with SDS reducing
190 the electrostatic repulsion of CTAB heads in the micellar aggregates (*i.e.* decreasing the surface
191 energy), and favoring the formation of assemblies with lower curvatures.^{19,26} This in turn,
192 facilitated the colloidal stabilization of COF oligomers and the final **TAPB-BTCA COF**
193 nanoparticles by the CTAB/SDS mixed surfactant system, even over extended periods of time.
194 Time-resolved SAXS experiments provided further insights into the growth mechanism of **TAPB-**
195 **BTCA COF** nanoparticles. SAXS spectra of the two micellar solutions containing the **TAPB** and
196 **BTCA** precursors (in the presence of acetic acid) indicated the existence of 4.8 ± 2 nm diameter
197 spherical micelles; comparable to what it was observed in pure CTAB/SDS (97:3) solutions (**Fig.**
198 **S11**). These data indicate that solubilization of COF precursors has a negligible effect on the size
199 and shape of the CTAB/SDS micellar aggregates. However, after mixing the two micellar solutions
200 loaded with COF precursors, clear changes in the SAXS profiles were observed as a function of
201 time. Scattering profiles at selected reaction times (5, 13, and 21 hours) are shown in **Fig. 2**, along
202 with their best fits obtained from the used scattering model (further details are provided in

203 Supplementary Materials). These three SAXS spectra describe three different regimes during the
204 progress of the reaction (**Fig. 2A-C** and **Fig. S12**). At short reaction times (5 hours in **Fig. 2A**),
205 SAXS profiles fit well to a disk-particle model with a radius of 6.4 nm and a thickness of 0.354
206 nm, which corresponds to a single layer of bare **TAPB-BTCA COF** (**Fig. S13A** and **Table S1**).
207 As the reaction proceeded (13 hours in **Fig. 2B**), SAXS data showed a significant increase in
208 intensity at low values of the scattering vector ($q < 1 \text{ nm}^{-1}$), together with the appearance of a broad
209 feature around 2 nm^{-1} , suggesting changes of electron density contrast (further discussion is
210 provided in the Supplementary Materials).²⁷ This spectrum could then be better fitted to a COF-
211 core@double-shell disk model, with a core thickness of 0.91 nm corresponding to a three-layered
212 **TAPB-BTCA COF** stack surrounded by surfactant molecules (**Fig. S13B** and **Table S1**). At longer
213 reaction times (21 hours in **Fig. 2C**), the SAXS profile showed a marked change at $q < 1 \text{ nm}^{-1}$, with
214 a clear slope variation at 0.5 nm^{-1} . This spectrum could also be described using a COF-
215 core@double-shell disk model, but with a core radius of 11 nm and a thickness of 3.74 nm (**Fig.**
216 **S13B** and **Table S1**). This thickness corresponds to ten-layered **TAPB-BTCA COF** stacks fully
217 covered by surfactant. Importantly, these extracted values were in good agreement with the overall
218 size of the colloidal particles as measured by DLS and cryo-TEM. It should be noted that the
219 formation of a compact surfactant layer around the COF nanoparticles is crucial for their
220 stabilization in the reaction mixture, preventing further growth and flocculation. Accordingly,
221 SAXS data suggest that after an initial phase of lateral growth by covalent polymerization, the
222 increase in size of **TAPB-BTCA COF** nanoparticles is essentially driven by the π - π stacking of
223 COF layers (**Table S1**). Coarse grained molecular dynamics (CG-MD) simulations of single-,
224 three- and ten-layered **TAPB-BTCA COF** particles were performed to gain further insight into the
225 forces driving the self-assembly process. The simulations were run in water as well as hexadecane

226 to simulate the hydrophobic environment of the micellar interior (see Supplementary Materials for
 227 further details about the CG model and simulations).



228
 229 **Fig. 2. Growth of TAPB-BTCA COF nanoparticles.** (A), (B) and (C) SAXS spectra of the reaction mixture at 5, 13
 230 and 21 hours, respectively. Experimental data (symbols) and best fits to the used scattering model (line). The insets
 231 illustrate the species measured at the three different regimes, with yellow disks representing the **TAPB-BTCA COF**
 232 core, red cylinders the hydrophobic tails of the surfactants, and blue spheres their polar heads. (D), (E) and (F)
 233 Snapshots of **TAPB-BTCA COF** assemblies comprising 1, 3 and 10 layers respectively, after CG-MD simulation in
 234 water. (G) Total energy for the simulations of **TAPB-BTCA COF** assemblies in water and hexadecane. Energies are
 235 normalized by dividing the total energy by the number of layers, N .

236

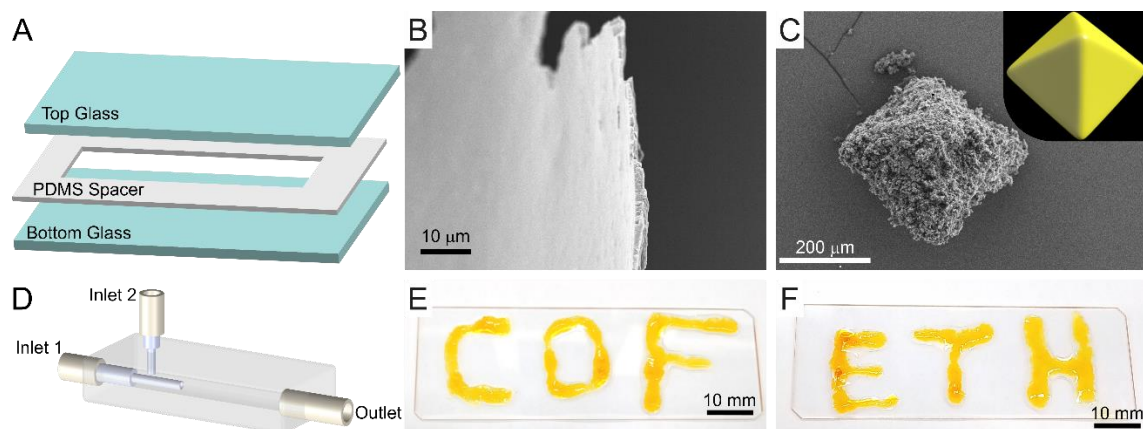
237 **Fig. 2 D-F** present snapshots of the equilibrated assemblies in water (see **Fig. S14** for the associated
238 simulations in hexadecane). Simulations confirmed the strong cooperativity in the interaction of
239 the COF layers in both solvents, with a significant reduction in the normalized energy per-layer for
240 the three and ten-layered **TAPB-BTCA COF** particles when compared to the isolated monolayer
241 (**Fig. S15**). The calculated energy of stabilization was similar in both solvents (**Fig. S15**). This
242 suggests that there is a strong preference for COF layers to aggregate, even within the hydrophobic
243 environment, due to a direct enthalpic contribution. However, when considering the total energy
244 of the simulated system (*i.e.* including the solvent contribution), there is a clear difference between
245 the behavior of the system in water or hexadecane (**Fig. 2G**). Specifically, COF layers are more
246 likely to aggregate in water (higher cooperativity), suggesting that in this case the driving force for
247 aggregation predominantly arises due to an increase in the water-water interactions upon COF
248 aggregation; a signature of the hydrophobic effect. In addition, MD simulations reveal a higher
249 flexibility of the COF single-layer, which deformed significantly during the simulations (e.g. **Fig.**
250 **2D** and **Fig. S14**) compared to the stacked systems (**Fig. 2E-F**). These data also explain the greater
251 tendency of surfactant molecules to interact with thicker assemblies (as measured by SAXS), since
252 rigid COF stacks have more extended hydrophobic patches (e.g. pore walls) than rippled single-
253 layers.

254 In addition to the importance of obtaining colloidal solutions of sub-20 nanometer COF particles
255 in water, the described methodology also offers new opportunities for particle processing. Indeed,
256 until now, a major limitation for the further implementation of COFs outside of laboratory
257 environments has been their unprocessable nature.²⁸ Here, we show that by controlling the
258 flocculation and aggregation of **TAPB-BTCA COF** nanoparticles in the reaction mixture (through
259 the addition of ethanol), 2D and 3D **TAPB-BTCA COF** shapes could be easily achieved. For

260 example, films of **TAPB-BTCA COF(s)** on the millimeter scale were prepared by confining a
261 concentrated reaction mixture into a home-made microengineered clamp (**Fig. 3A**), followed by
262 evaporation of the solvent. The concentrated reaction mixture was prepared by exchanging water
263 for ethanol (further details are provided in the Supplementary Materials). We observed that highly
264 uniform freestanding films with thicknesses of approximately 500 ± 10 nm were efficiently
265 obtained via this approach (**Fig. 3B**). Alternatively, reducing the size of the home-made
266 microengineered clamp to squares of 500 μ m lateral size or even changing its 2D shape to 3D
267 morphologies led to the generation of smaller **TAPB-BTCA COF(s)** films (**Fig. S16**) or 3D
268 octahedrons (**Fig. 3C** and Supplementary Materials). SEM analysis of these structures showed a
269 nanoparticulated texture similar to the one observed for **TAPB-BTCA COF(s)** (**Fig. S17**). These
270 data indicate that the processing steps allowed **TAPB-BTCA COF(s)** to be shaped into 2D and 3D
271 morphologies, with negligible reductions in the integrity of the COF material. Additionally, PXRD
272 patterns of these structures were identical to those previously reported in the literature for this COF
273 (**Fig. S18A**). Interestingly, the controlled diffusion of ethanol to the reaction mixture through a 3D
274 flow-focusing microfluidic device allowed us to generate a processable COF ink from the initial
275 colloidal solution. Indeed, the laminar flow conditions operating within such a device provided
276 control over the flocculation and aggregation of **TAPB-BTCA COF** nanoparticles (**Fig. 3D**).
277 Accordingly, a direct printing of **TAPB-BTCA COF(s)** onto surfaces was possible through the
278 tubing connected to the outlet of the microfluidic device (**Fig. 3E** and **3F** and **Video S1**). PXRD
279 analysis of the printed structures confirmed that **TAPB-BTCA COF(s)** was deposited (**Fig. S18B**).

280

281



282
 283 **Fig. 3. Processability of the reaction mixture.** (A) Schematic illustration of the home-made microengineered clamp
 284 used to generate **TAPB-BTCA COF(s)** films. (B) SEM image of the cross-section of a freestanding mm-sized film
 285 obtained using the setup shown in (A). (C) SEM image of a **TAPB-BTCA COF(s)** octahedron (500 μm edge). (D)
 286 Schematic illustration of the continuous 3D flow-focusing microfluidic device used to print **TAPB-BTCA COF(s)**.
 287 The reaction mixture was directly injected through inlet 1, while ethanol was introduced via inlet 2. (E) and (F)
 288 Photographs of "COF" and "ETH" printed with **TAPB-BTCA COF** on a planar surface using the device shown in (D).

289
 290 To demonstrate the generality of our method, we prepared another imine-based COF, namely **Tz-**
 291 **COF**²⁹ via the reaction of 2,4,6-tris(4-aminophenyl)-1,3,5-triazine and **BTCA** in a CTAB/SDS
 292 (97:3) mixture. SEM, DLS, and PXRD analysis clearly confirmed the formation of **Tz-COF**
 293 particles with a size distribution centered around 20 nm (**Fig. S19-S22**).³⁰ Permanent porosity was
 294 measured using BET analysis, with results agreeing with previously reported values for the same
 295 COF material (**Fig. S23**).³¹ Finally, it is significant to note that our method can be extended to
 296 MOFs. To demonstrate such generality, we synthesized a prototypical MOF that requires harsh
 297 conditions to crystallize, *i.e.* **MIL-100(Fe)**¹⁵. *In-situ* synchrotron X-ray diffraction measurements
 298 of the homogenous reaction mixture clearly confirmed the formation of **MIL-100(Fe)** (**Fig. S24**).
 299 Furthermore, DLS measurements of drop-cast reaction mixtures indicated a particle size
 300 distribution centered around 20 nm (**Fig. S25**). To the best of our knowledge, this is the smallest
 301 size reported for this biodegradable and non-toxic MOF.³² After flocculation of the colloid with

302 ethanol, PXRD and BET analysis of the resulting powder additionally confirmed the formation of
303 **MIL-100(Fe)**, (**Fig. S26** and **Fig. S27**, respectively). Surprisingly, and in spite of the nanometer
304 size of the generated **MIL-100(Fe)** particles, the measured BET surface area was high (1068 m²g⁻
305 ¹).

306 **Discussion**

307 In summary, we have demonstrated a mild procedure for the preparation of stable aqueous colloidal
308 solutions of crystalline imine-linked COF nanoparticles assisted by micelles of a *catanionic*
309 surfactant mixture. The micellar medium provides control over the growth of the COF crystallites,
310 which allowed us to reach the smallest size for COF particles among those reported so far.
311 Additionally, by a combination of experimental and computational studies, we were able to shed
312 light into the mechanism and forces underlying the growth of such COF colloids. Note that this
313 mechanistic study is unprecedented for imine-based COFs. Remarkably, the colloidal nature of the
314 formed imine-based COF nanoparticles enabled their processing into 2D and 3D shapes, as well as
315 the generation of an ink for their direct printing onto surfaces. Finally, to demonstrate the generality
316 of our method we extended it to the preparation of colloidal nanoparticles of other porous
317 crystalline materials, such as MOFs. We foresee that the preparation of chemically stable and easily
318 processable imine-based COF colloids will open the door to new applications of these materials,
319 for example in the field of functional devices, due to improved integration possibilities, or
320 biomedicine, thanks to improved bioavailability.

321

322 **References**

- 323 (1) Côté, A. P.; Benin, A. I.; Ockwig, N. W.; O’Keeffe, M.; Matzger, A. J.; Yaghi, O. M.
324 Porous, Crystalline, Covalent Organic Frameworks. *Science* **2005**, *310* (5751), 1166–1170.
325 <https://doi.org/10.1126/science.1120411>.
- 326 (2) Feng, X.; Ding, X.; Jiang, D. Covalent Organic Frameworks. *Chemical Society Reviews*
327 **2012**, *41* (18), 6010–6022. <https://doi.org/10.1039/C2CS35157A>.
- 328 (3) L. Segura, J.; J. Mancheño, M.; Zamora, F. Covalent Organic Frameworks Based on Schiff-
329 Base Chemistry: Synthesis, Properties and Potential Applications. *Chemical Society*
330 *Reviews* **2016**, *45* (20), 5635–5671. <https://doi.org/10.1039/C5CS00878F>.
- 331 (4) Huang, N.; Wang, P.; Jiang, D. Covalent Organic Frameworks: A Materials Platform for
332 Structural and Functional Designs. *Nature Reviews Materials* **2016**, *1* (10), 16068.
333 <https://doi.org/10.1038/natrevmats.2016.68>.
- 334 (5) Smith, B. J.; Parent, L. R.; Overholts, A. C.; Beaucage, P. A.; Bisbey, R. P.; Chavez, A. D.;
335 Hwang, N.; Park, C.; Evans, A. M.; Gianneschi, N. C.; et al. Colloidal Covalent Organic
336 Frameworks. *ACS Cent. Sci.* **2017**, *3* (1), 58–65. <https://doi.org/10.1021/acscentsci.6b00331>.
- 337 (6) Evans, A. M.; Parent, L. R.; Flanders, N. C.; Bisbey, R. P.; Vitaku, E.; Kirschner, M. S.;
338 Schaller, R. D.; Chen, L. X.; Gianneschi, N. C.; Dichtel, W. R. Seeded Growth of Single-
339 Crystal Two-Dimensional Covalent Organic Frameworks. *Science* **2018**, *361* (6397), 52–57.
340 <https://doi.org/10.1126/science.aar7883>.
- 341 (7) Wang, S.; McGuirk, C. M.; d’Aquino, A.; Mason, J. A.; Mirkin, C. A. Metal–Organic
342 Framework Nanoparticles. *Advanced Materials* **2018**, *0* (0), 1800202.
343 <https://doi.org/10.1002/adma.201800202>.
- 344 (8) Sakata, Y.; Furukawa, S.; Kondo, M.; Hirai, K.; Horike, N.; Takashima, Y.; Uehara, H.;
345 Louvain, N.; Meilikhov, M.; Tsuruoka, T.; et al. Shape-Memory Nanopores Induced in
346 Coordination Frameworks by Crystal Downsizing. *Science* **2013**, *339* (6116), 193–196.
347 <https://doi.org/10.1126/science.1231451>.
- 348 (9) Sindoro, M.; Yanai, N.; Jee, A.-Y.; Granick, S. Colloidal-Sized Metal–Organic
349 Frameworks: Synthesis and Applications. *Accounts of Chemical Research* **2014**, *47* (2),
350 459–469. <https://doi.org/10.1021/ar400151n>.
- 351 (10) DeBlase, C. R.; Dichtel, W. R. Moving Beyond Boron: The Emergence of New Linkage
352 Chemistries in Covalent Organic Frameworks. *Macromolecules* **2016**, *49* (15), 5297–5305.
353 <https://doi.org/10.1021/acs.macromol.6b00891>.
- 354 (11) Rodríguez- San- Miguel, D.; Yazdi, A.; Guillerm, V.; Pérez- Carvajal, J.; Puentes, V.;
355 Maspocho, D.; Zamora, F. Confining Functional Nanoparticles into Colloidal Imine-Based
356 COF Spheres by a Sequential Encapsulation–Crystallization Method. *Chemistry – A*
357 *European Journal* **2017**, *23* (36), 8623–8627. <https://doi.org/10.1002/chem.201702072>.
- 358 (12) Landis, W. J. Mineral Characterization in Calcifying Tissues: Atomic, Molecular and
359 Macromolecular Perspectives. *Connective Tissue Research* **1996**, *34* (4), 239–246.
360 <https://doi.org/10.3109/03008209609005267>.
- 361 (13) Hildebrand. Nanoscale Control of Silica Morphology and Three-Dimensional Structure
362 during Diatom Cell Wall Formation. *Journal of Materials Research* **2006**, *21*, 2689–2698.
363 <https://doi.org/10.1557/jmr.2006.0333>.
- 364 (14) Liu, X.; Theil, E. C. Ferritins: Dynamic Management of Biological Iron and Oxygen
365 Chemistry. *Accounts of Chemical Research* **2005**, *38* (3), 167–175.
366 <https://doi.org/10.1021/ar0302336>.

- 367 (15) Horcajada, P.; Surblé, S.; Serre, C.; Hong, D.-Y.; Seo, Y.-K.; Chang, J.-S.; Grenèche, J.-M.;
368 Margiolaki, I.; Férey, G. Synthesis and Catalytic Properties of MIL-100(Fe), an Iron(III)
369 Carboxylate with Large Pores. *Chemical Communications* **2007**, *0* (27), 2820–2822.
370 <https://doi.org/10.1039/B704325B>.
- 371 (16) Bellido, E.; GuilleVIC, M.; Hidalgo, T.; Santander-Ortega, M. J.; Serre, C.; Horcajada, P.
372 Understanding the Colloidal Stability of the Mesoporous MIL-100(Fe) Nanoparticles in
373 Physiological Media. *Langmuir* **2014**, *30* (20), 5911–5920.
374 <https://doi.org/10.1021/la5012555>.
- 375 (17) de la Peña Ruigómez, A.; Rodríguez- San- Miguel, D.; Stylianou, K. C.; Cavallini, M.;
376 Gentili, D.; Liscio, F.; Milita, S.; Roscioni, O. M.; Ruiz- González, M. L.; Carbonell, C.; et
377 al. Direct On-Surface Patterning of a Crystalline Lamellar Covalent Organic Framework
378 Synthesized at Room Temperature. *Chemistry – A European Journal* **2015**, *21* (30), 10666–
379 10670. <https://doi.org/10.1002/chem.201501692>.
- 380 (18) Tomašić, V.; Štefanić, I.; Filipović-Vinceković, N. Adsorption, Association and
381 Precipitation in Hexadecyltrimethylammonium Bromide/Sodium Dodecyl Sulfate Mixtures.
382 *Colloid and Polymer Science* **1999**, *277* (2–3), 153–163.
383 <https://doi.org/10.1007/s003960050380>.
- 384 (19) Kume, G.; Gallotti, M.; Nunes, G. Review on Anionic/Cationic Surfactant Mixtures. *J*
385 *Surfact Deterg* **2008**, *11* (1), 1–11. <https://doi.org/10.1007/s11743-007-1047-1>.
- 386 (20) Dwars, T.; Paetzold, E.; Oehme, G. Reactions in Micellar Systems. *Angewandte Chemie*
387 *International Edition* **2005**, *44* (44), 7174–7199. <https://doi.org/10.1002/anie.200501365>.
- 388 (21) Kraemer, E. O.; Dexter, S. T. The Light-Scattering Capacity (Tyndall Effect) and Colloidal
389 Behavior of Gelatine Sols and Gels. *J. Phys. Chem.* **1926**, *31* (5), 764–782.
390 <https://doi.org/10.1021/j150275a014>.
- 391 (22) Bail, A. L. Whole Powder Pattern Decomposition Methods and Applications: A
392 Retrospection. *Powder Diffraction* **2005**, *20* (4), 316–326.
393 <https://doi.org/10.1154/1.2135315>.
- 394 (23) Petříček, V.; Dušek, M.; Palatinus, L. Crystallographic Computing System JANA2006:
395 General Features. *Zeitschrift für Kristallographie-Crystalline Materials* **2014**, *229* (5), 345–
396 352.
- 397 (24) Li, W.; Han, Y.-C.; Zhang, J.-L.; Wang, B.-G. Effect of Ethanol on the Aggregation
398 Properties of Cetyltrimethylammonium Bromide Surfactant. *Colloid Journal* **2005**, *67* (2),
399 159–163. <https://doi.org/10.1007/s10595-005-0075-7>.
- 400 (25) Patterson, A. L. The Scherrer Formula for X-Ray Particle Size Determination. *Phys. Rev.*
401 **1939**, *56* (10), 978–982. <https://doi.org/10.1103/PhysRev.56.978>.
- 402 (26) Pucci, C.; Pérez, L.; Mesa, C. L.; Pons, R. Characterization and Stability of Catanionic
403 Vesicles Formed by Pseudo-Tetraalkyl Surfactant Mixtures. *Soft Matter* **2014**, *10* (48),
404 9657–9667. <https://doi.org/10.1039/C4SM01575D>.
- 405 (27) Pedersen, J. S. Analysis of Small-Angle Scattering Data from Colloids and Polymer
406 Solutions: Modeling and Least-Squares Fitting. *Advances in Colloid and Interface Science*
407 **1997**, *70*, 171–210. [http://dx.doi.org/10.1016/S0001-8686\(97\)00312-6](http://dx.doi.org/10.1016/S0001-8686(97)00312-6).
- 408 (28) Kandambeth, S.; Dey, K.; Banerjee, R. Covalent Organic Frameworks: Chemistry beyond
409 the Structure. *Journal of the American Chemical Society* **2019**, *141* (5), 1807–1822.
410 <https://doi.org/10.1021/jacs.8b10334>.
- 411 (29) Gao, Q.; Bai, L.; Zhang, X.; Wang, P.; Li, P.; Zeng, Y.; Zou, R.; Zhao, Y. Synthesis of
412 Microporous Nitrogen-Rich Covalent-Organic Framework and Its Application in CO₂

- 413 Capture. *Chinese Journal of Chemistry* **2015**, *33* (1), 90–94.
414 <https://doi.org/10.1002/cjoc.201400550>.
- 415 (30) Dong, J.; Wang, Y.; Liu, G.; Cheng, Y.; Zhao, D. Isoreticular Covalent Organic
416 Frameworks for Hydrocarbon Uptake and Separation: The Important Role of Monomer
417 Planarity. *CrystEngComm* **2017**, *19* (33), 4899–4904. <https://doi.org/10.1039/C7CE00344G>.
- 418 (31) Bai, L.; Phua, S. Z. F.; Lim, W. Q.; Jana, A.; Luo, Z.; Tham, H. P.; Zhao, L.; Gao, Q.; Zhao,
419 Y. Nanoscale Covalent Organic Frameworks as Smart Carriers for Drug Delivery. *Chem.*
420 *Commun.* **2016**, *52* (22), 4128–4131. <https://doi.org/10.1039/C6CC00853D>.
- 421 (32) Horcajada, P.; Chalati, T.; Serre, C.; Gillet, B.; Sebrie, C.; Baati, T.; Eubank, J. F.;
422 Heurtaux, D.; Clayette, P.; Kreuz, C.; et al. Porous Metal–Organic–Framework Nanoscale
423 Carriers as a Potential Platform for Drug Delivery and Imaging. *Nature Materials* **2010**, *9*
424 (2), 172–178. <https://doi.org/10.1038/nmat2608>.
- 425

426 **Acknowledgments:** We acknowledge DESY (Hamburg, Germany), a member of the Helmholtz
427 Association HGF, for the provision of experimental facilities. Synchrotron X-ray diffraction
428 experiments with COF-TAPB-BTCA were carried out at the beamline P02.1 PETRA III under the
429 proposal I-20170717 EC.

430 **Funding:** This work was supported by the European Union (ERC-2015-STG microCrysFact
431 677020), the Swiss National Science Foundation (Project no. 200021_181988), ETH Zürich and
432 Ministry of Science, Innovation and Universities MICINN (MAT2016-77608-C3-1P). A.E.P.P.
433 acknowledges a TALENTO grant (2017-T1/IND5148) from Comunidad de Madrid. D.M.
434 acknowledges financial support from the European Union (ERC-Co 615954). ICN2 is supported
435 by the Severo Ochoa program from the Spanish MINECO (Grant No. SEV-2017-0706).

436 **Competing interests:** A patent related to the work presented in this document has been filed.

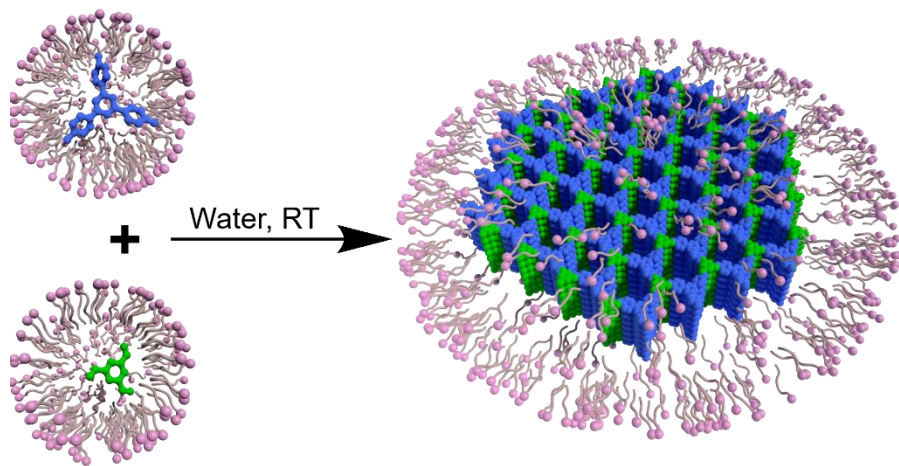
437 **Data and materials availability:** All data needed to evaluate the conclusions in the article is
438 present in the main text and supplementary materials.

439 **Supplementary Materials:** Materials and Methods; Supplementary Text; Figures S1-S31;
440 Tables S1; Movie S1.

441

442

443 **Table of Contents**



444